Available online at www.sciencedirect.com
ScienceDirect
Tectonophysics 427 (2006) 133–151
TECTONOPHYSICS
www.elsevier.com/locate/tecto

Ultrahigh temperature deformation microstructures in felsic granulites of the Napier Complex, Antarctica

Majbritt D. Lund [a,*], Sandra Piazolo [b,1], Simon L. Harley [c]

[a] Department of Life Sciences, University of Aalborg, Dk-9000 Aalborg, Denmark
[b] Department for Earth and Ocean Sciences, Liverpool University, UK
[c] School of Geosciences, Grant Institute, The King's Buildings, West Mains Road, Edinburgh EH9 3JW, Great Britain, UK

Received 14 July 2005; received in revised form 25 February 2006; accepted 11 May 2006
Available online 11 September 2006

Abstract

Detailed electron microscope and microstructural analysis of two ultrahigh temperature felsic granulites from Tonagh Island, Napier Complex, Antarctica show deformation microstructures produced at ~1000 °C at 8–10 kbar. High temperature orthopyroxene (Al ~7 wt.% and ~11 wt.%), exhibits crystallographic preferred orientation (CPO) and frequent subgrain boundaries which point to dislocation creep as the dominating deformation mechanism within opx. Two different main slip systems are observed: in opx bands with exclusively opx grains containing subgrain boundaries with traces parallel to [010] and a strong coupling of low angle misorientations (2.5°–5°) with rotation axes parallel to [010] the dominating slip system is (100)[001]. Isolated opx grains and grain clusters of 2–5 grains embedded in a qtz–fsp matrix show an additional slip system of (010)[001]. The latter slip system is harder to activate. We suggest that differences in the activation of these slip systems is a result of higher differential stresses imposed onto the isolated opx grains and grain clusters. In contrast to opx, large qtz grains (up to 200 μm) show random crystallographic orientation. This together with their elongate and cuspate shape and the lack of systematic in the rotation axes associated with the subgrain boundaries is consistent with diffusion creep as the primary deformation mechanism in quartz.

Our first time detailed microstructural observations of ultrahigh temperature and medium to high pressure granulites and their interpretation in terms of active deformation mechanisms give some insight into the type of rheology that can be expect at lower crustal conditions. If qtz is the mineral phase governing the rock rheology, Newtonian flow behaviour is expected and only low differential stress can be supported. However, if the stress supporting mineral phase is opx, the flow law resulting from dislocation creep will govern the rheology of the rock unit; hence, an exponential relationship between stress and strain rate is to be expected.

Keywords: Felsic granulites; Microstructure; Deformation mechanism; Orthopyroxene slip systems; Al diffusion; Ultrahigh temperature

1. Introduction

In order to model crustal scale processes such as mountain building it is crucial that the rheology of the lower crust is well constrained. Granulite terrains are good representatives of the lower crust (Carter and Tsenn, 1987), thus studying these should give some insight into the crustal strength at lower crustal conditions. In particular, ultrahigh grade metamorphic granulite terrains are windows to the lower continental crust, as they typically form at depths of 25–30 km, with peak metamorphic conditions above 900 °C and pressures between 7 and 13 kbar (Harley, 1989).

* Corresponding author. Fax: +45 96350558.
E-mail address: ml@bio.aau.dk (M.D. Lund).
[1] Presently at: Department of Geology and Geochemistry, Stockholm University, S-10691 Stockholm, Sweden.

0040-1951/$ - see front matter © 2006 Elsevier B.V. All rights reserved.
doi:10.1016/j.tecto.2006.05.022

Observations of microstructures including grain size and shape, and crystallographic relationships give constraints on the type and character of active deformation mechanisms. At lower crustal conditions the main expected deformation mechanisms are (1) solid state diffusion creep and (2) dislocation creep which result in a linear and exponential stress strain rate relationship respectively (e.g. Frost and Ashby, 1983). The active deformation mechanism may not only be a function of the temperature–pressure–fluid conditions during deformation but also of the spatial distribution of phases within the rock. Thus, to constrain the rheological character of the lower crust, the active deformation mechanisms and the influence of phase distribution relationships on such mechanisms need to be known.

Accordingly, in this study, the microstructural characteristics of two felsic granulites from Tonagh Island in the ultrahigh temperature (UHT) metamorphic terrain of the Napier Complex, Antarctica, are compared. Although both samples exhibit ultrahigh temperature mineral assemblages including Al-rich orthopyroxene (opx), sapphirine (spr), feldspars (fsp; antiperthite and plagioclase, (pl)), quartz (qtz) and ±garnet (grt) (all mineral abbreviations used according to Kretz (1983)), the spatial distribution of the main phases (i.e. qtz, fsp, opx) varies significantly. Analyses using a combination of optical light microscopy, electron microprobe and electron backscatter diffraction (EBSD) allows a characterization of the deformation microstructures and thus active deformation mechanisms of some of the main mineral phases. Results are then put into larger context of the rheology of felsic rocks at lower crustal conditions.

2. Geological setting and sample location

The Napier Complex (66°–68° S, 48°–57° E) is an Archean granulite facies terrain belonging to the East Antarctic Precambrian Shield which hosts UHT metamorphic rocks on a regional scale. A general description of the region is provided by Sheraton et al. (1980, 1987) and in reviews by Harley and Hensen (1990) and Harley (1998). Peak metamorphic conditions across the Napier Complex are >1000 °C at pressures from ~11 kbar in the southern part to ~6 kbar in the northern part (Harley, 1985; Harley and Motoyoshi, 2000; Hokada, 2001). Although, the exact time–temperature cooling history is not known in detail, it has been shown that the region underwent isobaric cooling to <850 °C at pressures of 6–8 kbar, according to analyses of retrograde mineral reactions and mineral corona development (e.g. Ellis, 1980; Harley, 1985; Ellis, 1987).

Tonagh Island itself is located at the southern end of Amundsen Bay (Fig. 1) and belongs to the central SE part of the Napier Complex. Tonagh Island rocks exhibit amongst the highest metamorphic grades found in the region (Harley, 1985). Re-integration of feldspar composition from feldspar exsolutions has indicated metamorphic peak conditions with temperatures above 1100 °C at Tonagh Island (Hokada, 2001) based on the two-feldspar thermometry of Fuhrmann and Lindsley (1988). Coexistence of metamorphic pigeonite and ferroaugite from East Tonagh Island also demonstrate peak conditions exceeding 980 °C at 6 to 8 kbar (Harley, 1987). According to Toyoshima et al. (1999), shearing during deformation event D_2 produced the dominant structural element of foliation (S_2) and mineral lineation (L_2) throughout Tonagh Island.

Two samples (DN33 and DN38) with different phase distribution and microstructure are studied and compared. Sample DN33 is from the western end of East Tonagh Island (Fig. 1) and comes from a pyroxene feldspathic gneiss in which pyroxene rich parts are strongly boudinaged as a result of layer parallel extension attributed to S_2 shearing. The sample (DN33) is taken from a moderately pyroxene rich part of the unit. Sample DN38 is from the SE part of the main Tonagh Island (Fig. 1) and is taken from a layered sequence dominated by felsic gneiss. The sample shows NS rotated and flattened mafic minerals (grt and spr) and opx augen pointing to a combination of coaxial and non-coaxial deformation.

3. Methods of analysis

3.1. Optical analysis

Optical analysis was used to identify the mineralogy, to measure the grain size and grain relationships in general and to select areas of special interest which were then used for more detailed analysis (see below). Polished thin sections (cut parallel to lineation and perpendicular to foliation) were examined both in plane polarised transmitted light and with crossed polars. Micrographs were taken with a Leica microscope equipped with a Leica DC300 digital camera and connected to a computer with image manager Leica IM50 v. 1.20.

3.2. Electron microprobe chemical spot and element map analysis

Chemical microprobe analysis was performed to identify the mineral chemistry and reactions for the PT calculations, and for comparisons with previous work.

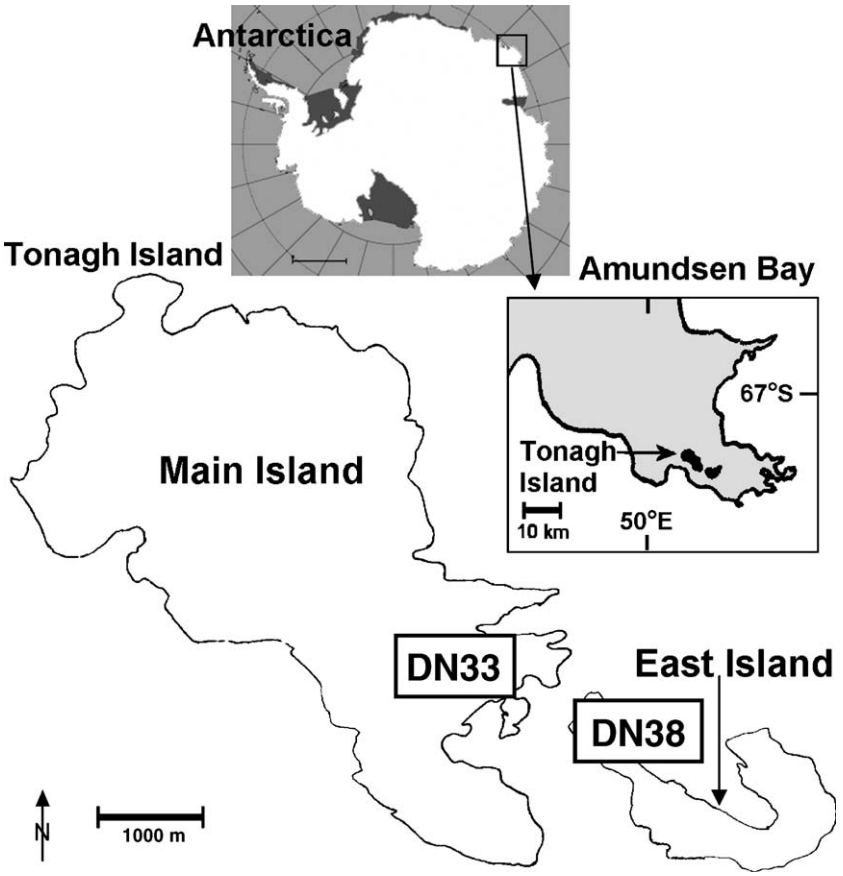

Fig. 1. The map shows Tonagh Island, Amundsens Bay, Napier Complex, Antarctica and the sample locations on the main island (DN33) and the east Tonagh Island (DN38) (modified from Osanai et al., 1999).

The microprobe mineral analyses were obtained by JEOL JXA-8200 Superprobe at the University of Copenhagen. 12 elements Al, Mn, Ti, K, Na, Si, Fe, Ba, Mg, Cr, Ca, F were analysed. Natural and synthetic standards were used for calibration (Al_2O_3 was used for Al, synthetic $MnTiO_3$ for Mn, rutile for Ti, K-feldspar for K, Albite for Na, Wollastonite for Si and Ca, hematite for Fe, $BaSO_4$ for Ba, "marjalathi" for Mg, synthetic Cr_2O_3 for Cr and "Apa-Willbo" for F). Except for feldspar all the mineral analyses were performed at 15 kV and 15 nA as point analyses in wavelength dispersive mode with a spot size of 5 μm. Three point analyses were measured in small local areas and averaged in the subsequent calculations. Grain analyses were made in both rims and apparent grain cores. Analyses of feldspars were obtained at 15 kV and 7 nA to minimize the evaporation of Na and antiperthite analyses were performed with focused beam (<1 μm) to obtain the most precise composition of both exsolution lamellae and host of the feldspars. In addition, elemental maps of selected opx grains in DN33 were produced for Al, Mg and Fe using the JEOL software.

3.3. Electron backscatter diffraction (EBSD) analysis

In-depth investigation of crystallographic orientations was performed by scanning electron microscope (SEM) based EBSD analysis using a field emission gun CamScan X500 Crystal Microprobe at the University of Liverpool. Polished thin sections were analysed at an accelerating voltage of 20 kV, beam current of 50 nA and a working distance of ~24 mm.

The electron backscatter diffraction patterns were automatically acquired and indexed using the Channel 5 acquisition software from HKL Technology, Denmark. For analysis 6–8 Kikuchi bands were matched with expected EBSD patterns using 80 to 110 theoretical reflectors. The accuracy of the crystallographic orientation of each measurement is typically better than 1°. The EBSD patterns were collected in regular grids where the

sampling step size varied from 1 μm to 20 μm. Data collection was done by stage scan and beam scan for large and small areas, respectively.

In the following analysis we define grains as areas enclosed fully by boundaries with misorientations >10°; boundaries with misorientations <10° are referred to as subgrain boundaries. The crystallographic orientations are displayed using pole figures, with equal area upper hemisphere projections, where the sample lineation is represented by X0, the foliation plane by XY and Z0 is the direction normal to the foliation plane. Based on the crystal symmetry a theoretical frequency pattern of misorientations can be calculated (e.g. Wheeler et al., 2001) and compared to the measured misorientation frequencies in the analysed samples (cf. Fig. 5). Misorientation angles are calculated between immediately neighbouring analysis pairs and between randomly picked analysis pairs in the data set.

Detailed EBSD analyses were concentrated on opx and qtz. In DN33 opx have been analysed in opx bands and qtz in the interlobate matrix between the bands. In DN38 the analysed areas are taken from layer II (opx embedded in a qtz) and layer III (qtz).

4. Results

4.1. General microstructural description using optical analysis

Both samples exhibit mineral assemblages of opx ~30 area%, ±grt (~12 area% in DN38), spr ~3–7 area %, fsp (antiperthite, plagioclase) ~45 area% and 35 area %, respectively, qtz ~20 area%; main accessory minerals are rutile (rt) and spinel (spl). Spr occurs in layers and lenses parallel with the main gneissic fabric and consist of spr+pl dominantly. Elongated opx grains and domains form a strong mineral lineation.

In DN33 opx grains are dominantly arranged in monomineralic bands separated by quartzo–feldspathic domains as well as near pure qtz domains (Fig. 2A,B and C). The average aspect ratio of individual opx grains in opx bands is ~2 with a maximum aspect ratio of 5.3. Several opx grains show straight intergranular boundaries perpendicular to the grain elongation (Fig. 2D), which are evenly distributed along and across opx bands. The quartzo–feldspathic matrix is made up of inequigranular and interlobate fsp, primarily antiperthite (Fig. 2E), interconnected with anhedral, moderately elongate qtz showing both undulose extinction and occasional subgrain boundaries (Fig. 2F).

The mineral phase distribution in sample DN38 is significantly different to that of DN33. Three different layers can be distinguished (Fig. 3A). Layer I includes large opx augen surrounded by inequigranular pl grains. The large opx augen are between 300 μm and 1.5 mm across and are made of either individual large grains or elongate clusters of 3–35 opx grains. In places, rims of grt at opx–pl and outermost opx–opx boundaries are seen (Fig. 3B). These rims are not elongated and individual grt grains show no shape preferred orientation. Spr is present in this part of the sample and is occasionally overgrowing spl (Fig. 3F). Layer II is dominated by shape preferred orientation of either individual large opx grains or elongate clusters of 2–5 opx grains parallel to the sample lineation (Fig. 3C and D) in a fsp–qtz matrix which also includes individual grt grains. The average aspect ratio of opx grains is ~2 with a maximum aspect ratio of 5.2. Layer III is formed by an interconnected network of interlobate antiperthite, pl and qtz which shows some undulatory extinction separated by lineation-parallel qtz ribbons (Fig. 3F). The qtz ribbons occasionally have cuspate boundaries. The ribbons are commonly 150–400 μm wide, and this also represents the range of widths of individual qtz grains within ribbons. Most ribbons show lengths of over 1 mm long and are built-up of several grains along the length of the crystals. Individual grains show aspect ratios between 2 and 5, with an average of ~3.1. Ribbon grains show some undulose extinction and subgrain boundaries are often oriented oblique to ribbon boundaries (Fig. 3E). Such subgrain boundaries are most frequent within the largest ribbon grains; in contrast, some small ribbon grains are almost devoid of subgrain boundaries. Occasionally small fsp grains are included in the quartz ribbons.

Note that we chose to focus our investigations on the character of opx grains in layer II as here the spatial distribution of opx, qtz and fsp is significantly different to that of sample DN33.

4.2. Chemical composition of main mineral phases

Antiperthite is the dominant fsp in both samples. The pl (host) composition range is X_{An} 0.18–0.22 in DN33 (Table 1) and X_{An} 0.29–0.33 in DN38 (Table 2) while the K-feldspar (kfs) exsolution lamella range between X_{Or} 0.90 and 0.98 in both samples. Antiperthite is usually rimmed by pure pl with a slightly higher X_{An} composition, i.e. 0.27 (DN33) and 0.40 (DN38).

In both samples opx is a solid solution in the system FeO-MgO-Al_2O_3-SiO_2 with minor amounts of CaO and MnO (~0.01 a.p.f.u.), and with a Mg/(Mg+Fe) average of 72% in both samples (Tables 1 and 2). Opx overgrown by grt in DN38 has a higher Mg content adjacent to the

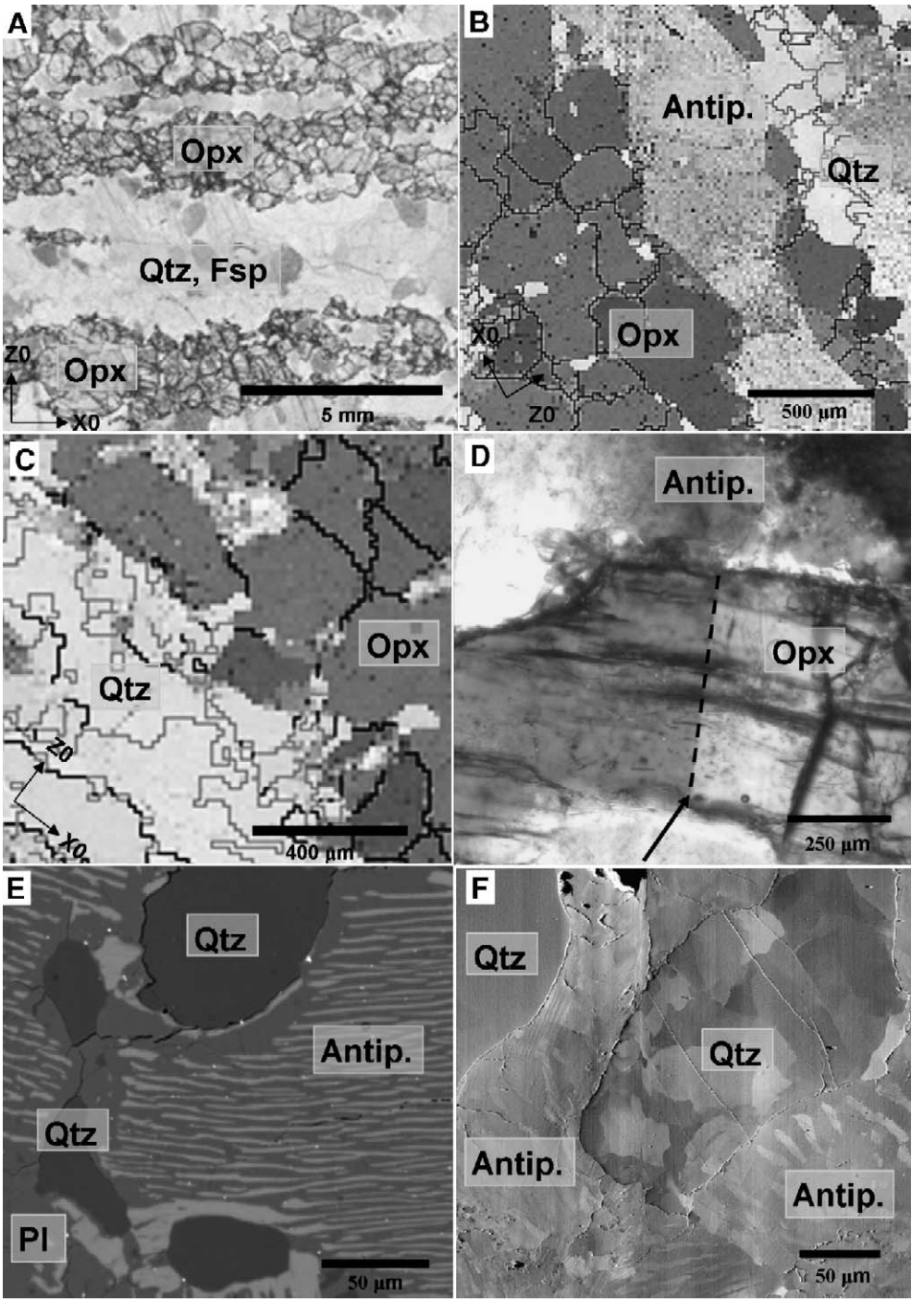

Fig. 2. Representative microstructures of sample DN33: A) Optical, plain light overview micrograph showing opx bands separated by quartzo–feldspathic domains. B) EBSD map of opx bands (dark grey), antiperthite and qtz bands, black lines are grain boundaries with a misorientation above 10°. C) EBSD map showing an analysed opx band with adjacent qtz band, step size is 20 μm; black lines are grain boundary misorientations above 10°. D) Example of straight subgrain boundary of opx in DN33 (marked by a black arrow), optical plain light. E) Close-up of quartzo–feldspathic domain with exsolution microstructures in feldspar and slightly elongate qtz grain; BSE image. F) Illustration of a qtz grain with significant substructure; forescatter image where different grey levels signify slight differences in crystallographic orientation.

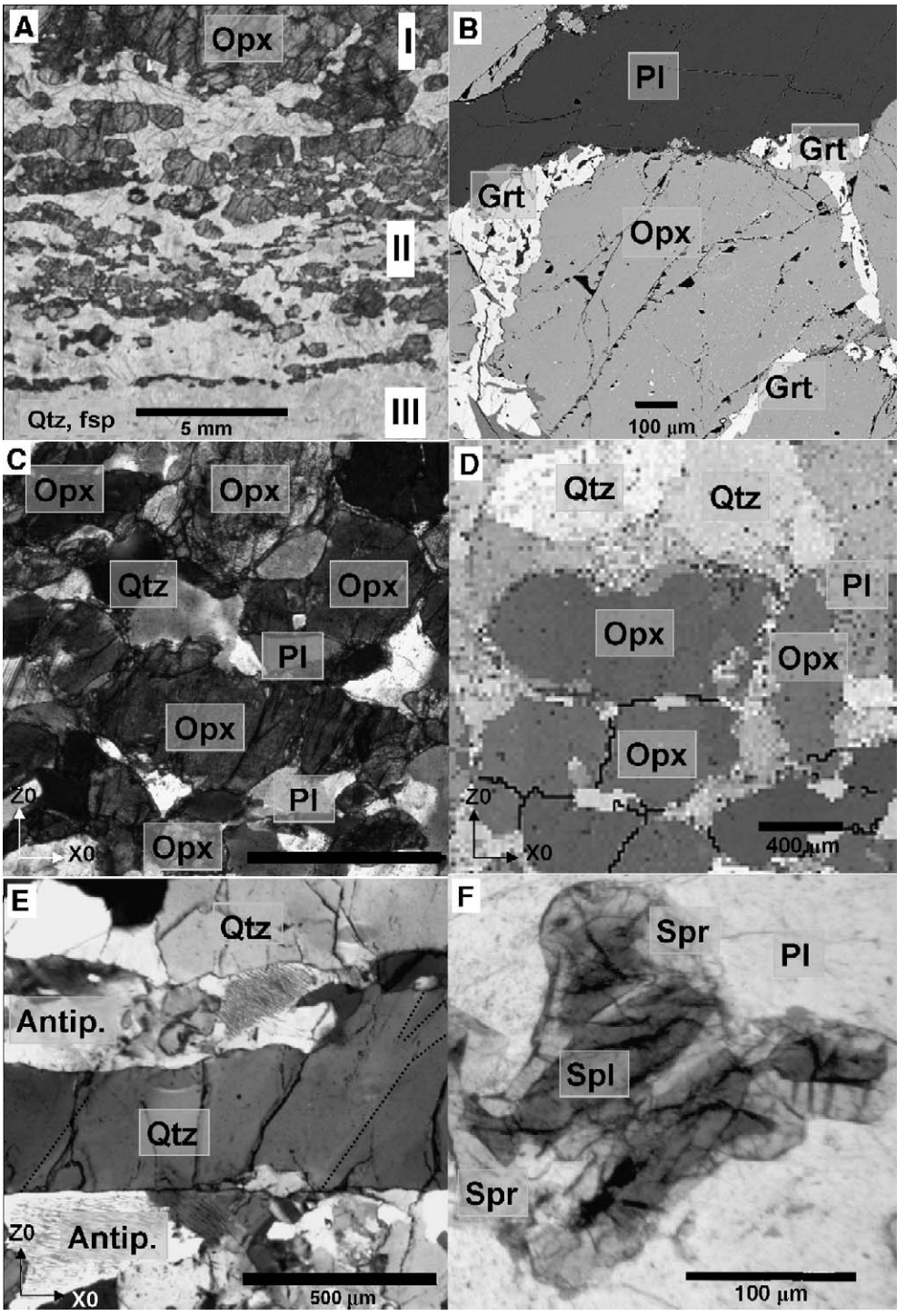

Fig. 3. Representative microstructures of sample DN38 are shown. A) Optical, plain light overview micrograph of DN38 showing: Layer I — opx augens and pl matrix; Layer II — shape preferred orientations of opx grains and grain clusters and quartzo–feldspathic matrix; Layer III — quartzo–feldspathic matrix with qtz ribbons. B) Example of grt reaction rims along high Al opx augens in Layer I of DN38, BSE image. C) Optical, plain light micrograph of the opx arrangement in layer II, scale bar equals 500 μm. D) EBSD map of opx in layer II, step size of 20 μm and black lines are grain boundary misorientation above 10°, opx: dark grey; qtz: almost white; fsp: light grey. E) Optical, plain light micrograph of a qtz ribbon in layer III indicating subgrain boundaries oblique to the ribbon boundary. F) Optical, plan light micrograph of spr overgrowth of spl found in layer I.

Table 1
Representative mineral chemistry from microprobe analyses of DN33

Sample	DN33						Antiperthite		Antiperthite	
Mineral	Opx core		Opx rim		Spr		Pl (host)		K-fsp (lam)	
Wt.%		S.D.		S.D.		S.D.		S.D.		S.D.
SiO_2	50.641	0.314	51.597	0.110	14.224	0.131	63.117	0.382	63.935	0.046
Al_2O_3	7.041	0.084	5.065	0.220	60.972	0.455	22.902	0.316	18.288	0.076
TiO_2	0.104	0.013	0.054	0.038	0.028	0.018	–	–	–	–
Cr_2O_3	–	–	–	–	–	–	–	–	–	–
FeO	17.368	0.171	17.879	0.206	8.138	0.327	0.061	0.021	–	–
MgO	24.057	0.210	24.918	0.104	15.980	0.152	–	–	–	–
MnO	0.317	0.027	0.327	0.054	0.092	0.063	–	–	–	–
K_2O	–	–	0.010	0.008	–	–	0.132	0.016	15.108	0.156
Na_2O	–	–	–	–	0.016	0.018	9.270	0.102	0.833	0.218
CaO	0.049	0.012	0.055	0.012	0.018	0.007	4.215	0.044	0.079	0.025
BaO	–	–	–	–	–	–	–	–	0.603	0.127
F	–	–	–	–	–	–	–	–	–	–
Total	99.557	0.625	99.905	0.465	99.468	0.611	99.851	0.508	98.986	0.127
Formula proportion of cation										
O atoms	6		6		20		8		8	
Si	1.845	0.011	1.880	0.004	1.703	0.016	2.799	0.012	2.988	0.002
Al	0.302	0.002	0.217	0.005	8.605	0.032	1.197	0.015	1.013	0.004
Ti	0.003	0.001	0.001	0.001	0.002	0.002	–	–	–	–
Cr	–	–	–	–	–	–	–	–	–	–
Fe	0.529	0.005	0.545	0.006	0.815	0.033	0.002	0.001	–	–
Mg	1.307	0.011	1.353	0.006	2.852	0.027	–	–	–	–
Mn	0.010	0.001	0.010	0.002	0.009	0.006	–	–	–	–
K	–	–	–	–	–	–	0.007	0.001	0.901	0.010
Na	–	–	–	–	0.004	0.002	0.797	0.007	0.076	0.007
Ca	0.002	0.001	0.002	0.001	0.002	0.001	0.203	0.003	0.004	0.001
Ba	–	–	–	–	–	–	–	–	0.011	0.002
F	–	–	–	–	–	–	–	–	–	–
Total	3.998	0.033	4.008	0.025	13.992	0.010	5.005	0.021	4.993	0.012
An							0.201	0.124	0.004	0.325
Ab							0.791	0.124	0.077	0.325
Or							0.007	0.124	0.919	0.325

Values are averaged of 3 point analyses made in small local areas; standard deviation is given (S.D.).
An=Ca/(Na+K+Ca); Ab=Na/(Na+K+Ca); Or=K/(Na+K+Ca).

grt than within the grain core. The Al content in both samples is high: in DN33 it is 7 wt.% Al and in DN38 it is 11 wt.%. Such highly aluminous opx is characteristic in many ultrahigh temperature opx-bearing granulite facies rocks (i.e. Harley and Hensen, 1990). Elemental mapping and point analyses (Tables 1 and 2) of selected opx grains in DN33 show a homogenous Fe and Mg distribution, whereas Al signatures show distinct distribution patterns: (a) a decrease in Al content towards the grain boundaries (cf. Fig. 4) and (b) distinct Al decrease along straight subgrain boundaries with ~4° misorientation (cf. Fig. 5).

4.3. Thermobarometric calculations

Thermobarometric calculations to estimate peak metamorphic temperatures of sample DN38 (Tables 1 and 2) made use of the composition of coexisting phases opx and grt. The equilibrium expressed by end members of grt and opx including Al_2O_3 is described by the equation:

$$\text{In general}: \text{Alm} + \text{Prp} = 3\text{Fs} + 3\text{En} + 2\text{Al}_2\text{O}_3 \quad (3)$$

$$\text{Fe} - \text{Al}_{\text{Tsch}}: \text{Alm} = 3\text{Fs} + \text{Al}_2\text{O}_3 \quad (3.1)$$

$$\text{Mg} - \text{Al}_{\text{Tsch}}: \text{Prp} = 3\text{En} + \text{Al}_2\text{O}_3 \quad (3.2)$$

Specifically, Fe–Mg exchange thermometers (Harley, 1984; T(H84), Ganguly et al., 1996; T(G96), Carswell and Harley, 1989; T(CH89) and Bhattacharya et al., 1991; T(B91)) and the Fe–Tschermaks exchange (Fe–Al_{Tsch}) in opx (Aranovich and Berman, 1997: T(AB97)) were used (see Table 3). Peak pressure and recast temperatures were estimated using the Mg–Tschermaks exchange in opx in coexistence with grt (Wood, 1974; P

Table 2
Representative mineral chemistry from microprobe analyses of DN38

Sample	DN38											
Mineral	Opx core		Opx rim1		Spr		Grt		Fspr Pl (host)		Fspr K-fsp (lam)	
Wt.%		S.D.		S.D.		S.D.		S.D.		S.D.		
SiO_2	48.516	1.106	50.191	0.349	13.253	0.298	39.832	0.196	60.911	0.089		
Al_2O_3	10.731	0.822	8.131	0.199	62.039	0.252	23.141	0.181	24.628	0.294	18.424	0.130
TiO_2	0.056	0.028	0.161	0.212	0.054	0.028	0.036	0.026	–	–		
Cr_2O_3	0.769	0.220	0.410	0.080	0.869	0.093	0.244	0.013	–	–	0.028	0.021
FeO	17.080	0.049	17.009	0.269	8.564	0.245	22.043	0.182	–	–	–	–
MgO	23.832	0.339	24.123	0.118	15.513	0.072	12.864	0.196	–	–	–	–
MnO	0.363	0.025	0.342	0.075	0.162	0.013	1.586	0.061	–	–	–	–
K_2O	–	–	–	–	–	–	–	–	0.178	0.097	15.539	0.296
Na_2O	0.016	0.020	–	–	0.014	0.007	–	–	7.978	0.034	0.651	0.121
CaO	0.032	0.004	0.050	0.009	–	–	1.287	0.052	6.373	0.214	0.144	0.068
BaO	–	–	–	–	–	–	–	–			0.462	0.029
F	–	–	–	–	–	–	–	–			–	–
Total	101.395	0.422	100.445	0.689	100.468	0.222	101.321	0.281	99.757	0.478	99.115	0.349
Formula proportion of cation												
O atoms	6		6		20		12		8		8	
Si	1.769	0.040	1.814	0.025	1.579	0.035	2.964	0.029	2.699	0.011	2.985	0.006
Al	0.429	0.017	0.346	0.013	8.714	0.018	2.029	0.024	1.295	0.013	1.014	0.004
Ti	0.002	0.001	0.004	0.012	0.005	0.002	0.002	0.003	–	–	–	–
Cr	0.017	0.018	0.012	0.003	0.082	0.004	0.014	0.001	–	–	0.001	0.001
Fe	0.512	0.001	0.514	0.008	0.854	0.024	1.372	0.011	–	–	–	–
Mg	1.288	0.018	1.299	0.006	2.756	0.013	1.427	0.022	–	–	–	–
Mn	0.012	0.001	0.010	0.002	0.016	0.001	0.100	0.004	–	–	–	–
K	–	–	–	–	–	–	–	–	0.010	0.005	0.917	0.018
Na	0.002	0.001	–	–	0.003	0.001	–	–	0.690	0.001	0.059	0.011
Ca	0.001	0.000	0.002	0.000	–	–	0.103	0.004	0.305	0.009	0.007	0.003
Ba	–	–	–	–	–	–	–	–	–	–	0.009	0.001
F	–	–	–	–	–	–	–	–	–	–	–	–
Total	4.032	0.047	4.001	0.032	14.009	0.049	8.011	0.045	5.001	0.019	4.994	0.022
Xprp							0.475	0.059				
Xalm							0.457	0.059				
An									0.303	0.539	0.007	0.504
Ab									0.687	0.539	0.060	0.504
Or									0.010	0.539	0.933	0.504

Values are averaged of 3 point analyses made in small local areas; standard deviation is given (S.D.).
X_{prp}=Mg/(Fe+Mg+Ca+Mn); X_{alm}=Fe/(Fe+Mg+Ca+Mn); An=Ca/(Na+K+Ca); Or = L/(Na + K + Ca).

(W74), Harley and Green, 1982; P(HG82) and Harley, 1984) (see Table 3).

All above calculations are made in two sets since the Al distribution may be expressed either as X_{Al}=Al/2 or $Al_{(site)}$=(Al+Si+2Ti+Cr)−2. X_{Al} represent the ideal theoretical Tschermak substitution between $^{[4]}$T and $^{[6]}$M: this method will overestimate the octahedral Al content if other R^{3+} are also present. $Al_{(site)}$ assumes full occupancy of $^{[4]}$T and allows occupancy R^{3+} also by Ti and Cr in the octahedral sites. To account for late Fe–Mg inter-diffusion, the mineral compositions have been re-calculated to arrive at a self-consistent pressure of 8 kbar which is consistent with nearby rocks bearing stable osumilite (Osanai et al., 1999). Therefore the estimations of peak metamorphic conditions fall in the range of 965–1040 °C at 8 kbar (see retrieved results in Table 3).

A further constraint on the minimum peak temperature is derived from the re-integration of antiperthitic fsp based on the two-feldspar thermometry of Fuhrmann and Lindsley (1988) using SOLVCALC (Wen and Nekvasil, 1994). Re-integrated compositions of antiperthite give minimum temperatures of 950 °C (DN33) to 1035 °C (DN38) (Table 3). In addition, the stable peak metamorphic assemblage of grt, opx, spr, qtz and fsp indicates temperatures above 1000 °C (Sheraton et al., 1987; Harley, 1998; Harley and Motoyoshi, 2000). Furthermore, observed spr overgrowth of spl (DN38) points to prograde mineral reaction at temperatures above 950 °C and pressures of 9 kbar or above (Harley, 1989).

$$\mathrm{Spl} + \mathrm{Pl(Kfs)} \rightarrow \mathrm{Spr} + \mathrm{Pl(Kfs)} \quad (4)$$

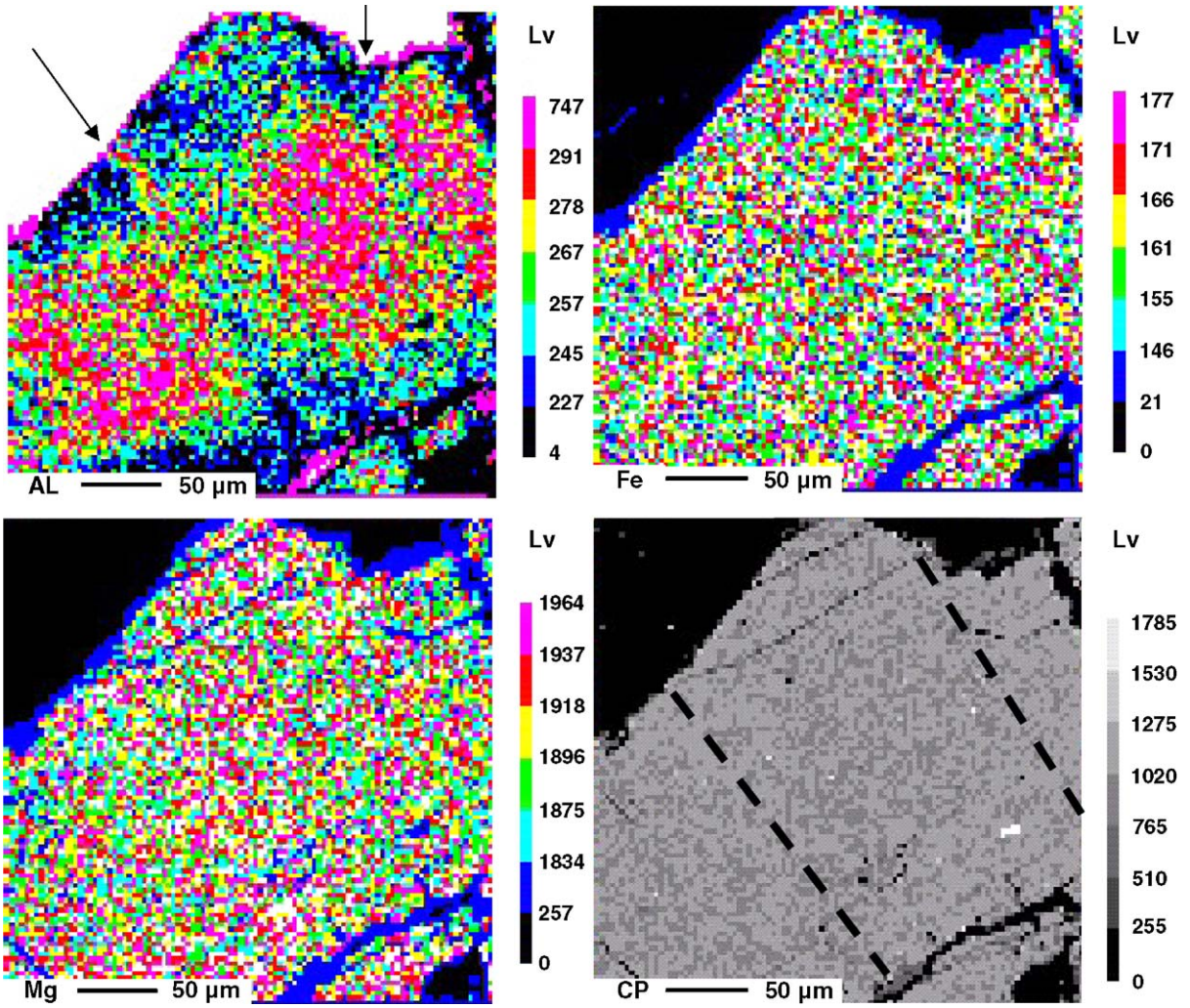

Fig. 4. Results from element mapping of Al, Fe, and Mg in an opx grain from DN33 including straight subgrain boundaries across the length of the grain. The trace of the subgrain boundaries can be recognised in the Al map, and are marked by two arrows and a stippled line. Legends show the signal level (Lv) constraining the scale at the individual maps shown.

Part of the retrogression path is constrained by the grt reaction rims between opx and other aluminium phases such as pl (Fig. 3B; DN38) (i.e. Harley, 1998).

$$\text{High Al–Opx} \rightarrow \text{Low Al–Opx} + \text{Grt} \quad (5)$$

By constraining the pressures to 6 kbar according to previous studies (i.e. Harley, 1985), estimations using the same thermometers as mentioned above (Eq. (3)) indicate retrogression at around 800–880 °C (see Table 3).

4.4. Crystallographic characteristics

4.4.1. Orthopyroxene

Both samples show a grain elongation which is roughly parallel to [001] and a size independent crystallographic preferred orientation for opx (Figs. 6 and 7). In sample DN33 [001] is parallel to the lineation (X0), poles to (100) are sub-parallel to the normal direction of the foliation plane (Z0), and poles to (010) are sub-parallel to the plane (XY) (Fig. 6). In contrast, in layer II of DN38 [001] is parallel to the lineation (X0), (010) is sub-parallel to Z0 and (100) is sub-parallel to the (XY) plane (Fig. 7).

Both samples show high frequency of subgrain boundaries (misorientation angles <10°) (Fig. 8). In sample DN33 opx has a high frequency of grain boundaries below 20° misorientation for neighbouring grain pairs and a higher frequency of grain boundaries with 20°–60° misorientation among random grain pairs. In contrast, DN38 shows a neighbouring pair distribution with significantly higher frequencies of high angle

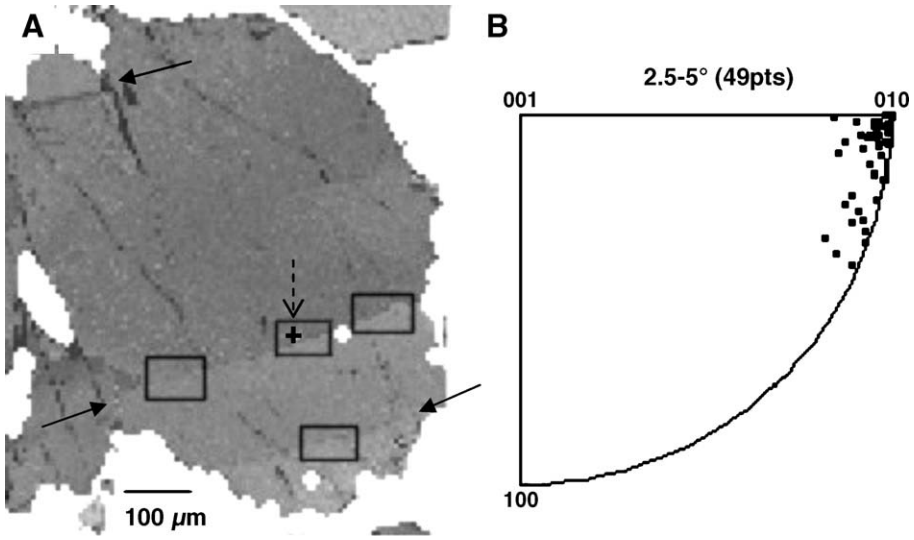

Fig. 5. EBSD analyses of opx demonstrating straight subgrain boundaries show the boundaries to have misorientation angles between 2.5 and 5° and preferred rotation axis of [010]. The long axis of the grain is parallel to [001] and the trace of the subgrain boundary parallel to (010). A) Misorientation variations within the opx grain; the grain is grey shaded according to misorientation to a reference crystallographic orientation (black cross). The maximum misorientation is 10°. Traces of straight subgrain boundaries are pointed out by three arrows. B) Rotation axes of neighbouring pair misorientation data taken from the four boxes marked in A) shown in inverse pole figures in crystal coordinates.

boundaries. For the random pair distribution, grain boundary angles similar to the theoretically random distribution are observed.

In DN33 specific misorientation angle ranges are associated with clear preferred rotation axes (Fig. 8B and C); for 10°–20° it is the axis parallel to (010) and at angles around 60° it is parallel to (001). Observed straight subgrain boundaries (cf. Fig. 4 and Section 4.2) are normal to the grain elongation which is parallel to [001]. Hence, the trace of these boundaries is parallel to (010). In addition, a strong coupling of low angle misorientations (2.5°–5°) with rotation axes parallel to [010] is observed (Fig. 5). In DN38, though, only low angle boundaries (2–10° misorientation) show a noticeable preferred rotation axis parallel either to [010] or to [100], whilst systematic straight subgrain boundaries are absent.

4.4.2. Quartz

Qtz is found in the quartzo–feldspathic matrix in both samples with grain sizes between 50 and 200 μm.

Table 3
Summary of the thermobarometric calculations of DN38 based on Al solubility in opx and re-integrated ternary feldspar compositions from both samples (re-int. Fspr)

Method all T=°C	P(nom) Kbar	T (H84)	T (LG88)	T (CH89)	T (B91)	T (G96)	P (W74)	P (HG82)	T(HG82)[a] T Mg–Al	T(AB97) T Fe–Al	Re-int. Fspr	Re-int. Fspr
DN38 retrieved											Min	Max
Opx core, Al/2	10	959	1053	993	956	1051	10.19	9.67	1061	1018		
Opx core, Al/2	8	945	1039	978	939	1037	8.50	8.30	993	975		
Opx core, Al(site)	10	956	1053	993	956	1051	10.92	10.24	1042	1006		
Opx core, Al(site)	8	945	1039	978	939	1037	9.19	8.82	976	964		
DN33											950	975
DN38											1000	1035
DN38												
Opx rim, Al/2	6	781	860	809	784	859	3.27	3.51	879	854		
Opx rim, Al(site)	6	781	860	809	784	859	3.92	4.01	862	842		

Thermobarometers used is labelled and referenced in the text.
[a] Is the Mg–Al thermobarometer recast as a thermometer.

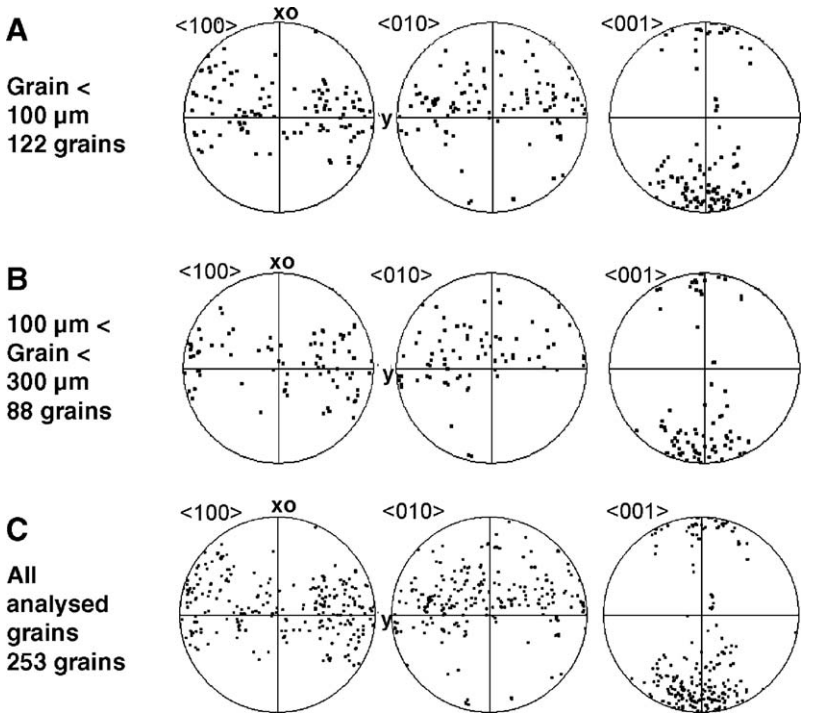

Fig. 6. Crystallographic orientations of opx grains (DN33) shown in equal area upper hemisphere projections. A) Crystallographic orientations of grains smaller than 100 μm in diameter. B) Crystallographic orientations of grains between 100 and 300 μm in diameter. C) Full dataset including all grain sizes.

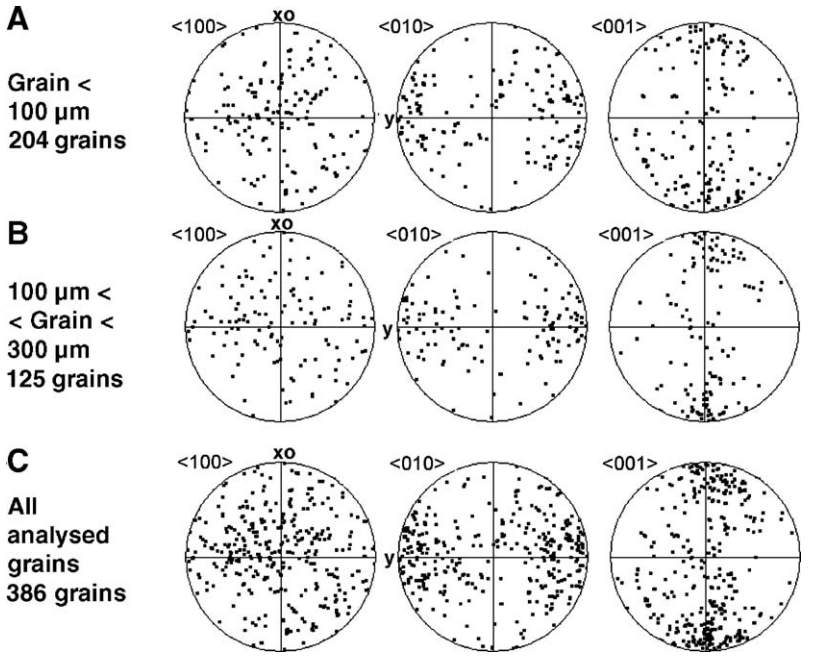

Fig. 7. Crystallographic orientation of opx grains (DN38) shown in equal area upper hemisphere projections. A) Crystallographic orientations of grains smaller than 100 μm in diameter. B) Crystallographic orientations of grains between 100 and 300 μm in diameter. C) Full dataset including all grain sizes.

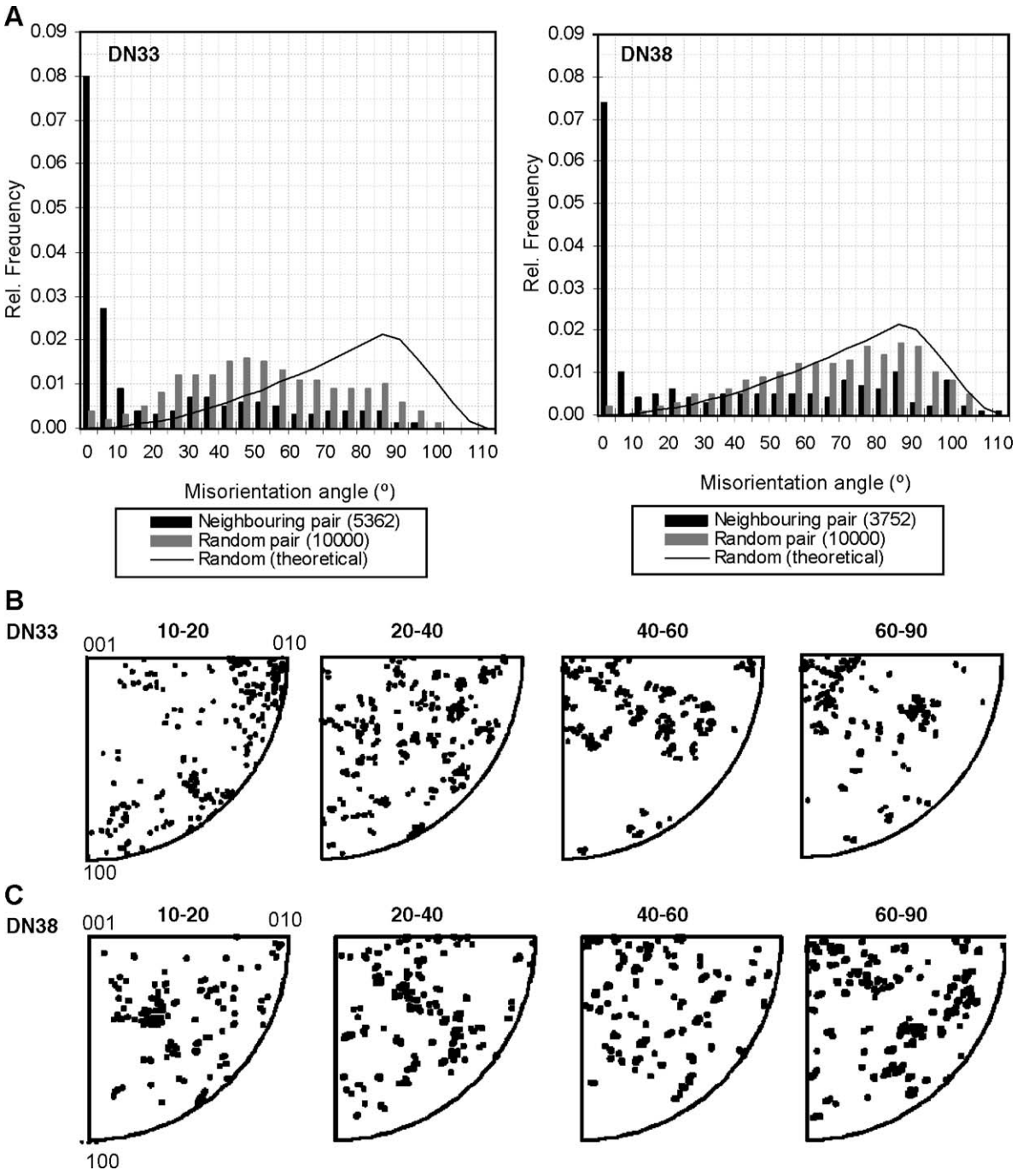

Fig. 8. Misorientation angle distributions and associated rotation axis distributions for opx grains measured in the two samples. The theoretical frequency curve is shown as a black line and the two types of misorientation angle distributions are illustrated by block diagrams in dark grey and white, respectively (see text for further explanations). A) Misorientation angle distributions, DN33 and DN38. B) Rotation axes shown in inverse pole figures in crystal coordinates for randomly picked grain pairs in DN33. C) Rotation axes shown in inverse pole figures in crystal coordinates for randomly picked grain pairs in DN38. Rotation axes are grouped according to the misorientation angle, shown for misorientation between 10° and 90°.

In addition, in DN38 qtz is also present as ribbons within the quartzo–feldspathic matrix. EBSD analyses of lobate, slightly elongated matrix qtz grains and qtz ribbons show no crystallographic preferred orientation irrespective of the grain size (Fig. 9). For both matrix and ribbon qtz, the misorientation angle distribution is

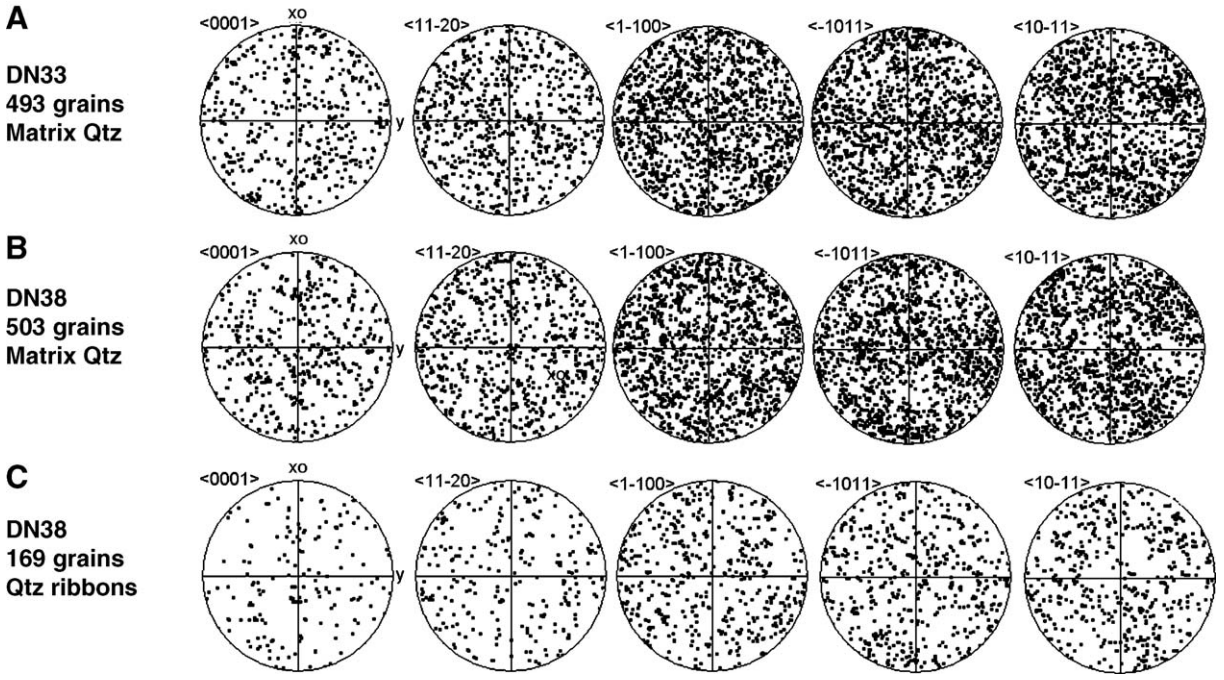

Fig. 9. Crystallographic orientations of qtz grains are shown. The crystallographic directions shown in the stereographic projections are: [0001], [11–20], [1–100], [–1011], and [10–11]. A) Orientations of matrix grains from DN33, B) orientations of matrix quartz grains from DN38 and C) orientations within qtz ribbons of DN38.

close to theoretical if randomly picked qtz grain pairs are analysed (Fig. 10). For neighbouring grain pairs the misorientation angle distribution shows a higher frequency of both subgrain boundaries and boundaries with 60° misorientations than the theoretically calculated distribution (Fig. 10). Subgrain boundary rotation axes show no systematic crystallographic alignment. In contrast, rotation axes of misorientation angles around 60° are strongly aligned with the [0001] direction (matrix grains: Fig. 10A and B; ribbon grains: Fig. 10C and D). This rotation is consistent with Dauphiné twinning, i.e. twinning by an 180° rotation around [0001]. The spatial distribution of these Dauphiné twins is not correlated to any specific microstructural feature, such as grain asperities or high angle grain boundaries.

5. Interpretation and discussion of observed microstructures

5.1. Condition of metamorphism and deformation

The aluminium solubility in opx, re-integration of antiperthite composition and peak metamorphic stable mineral assemblages all indicate peak metamorphic conditions of ~965–1050 °C at 8–10 kbar, i.e. ultrahigh temperature metamorphism. This result agrees well with findings of Hokada (2001), Harley (1989) and Harley and Hensen (1990). Retrogression occurred between 800 and 900 °C at 6 kbar which is in agreement with retrogression estimates of Ellis (1980, 1987) and Harley (1985).

Although we observe the latter retrograde reaction, deformation microstructures described and discussed below are attributed to have formed at or near peak metamorphic conditions. Several pieces of evidence support this interpretation: (a) element distribution pattern in high temperature opx, (b) undeformed grt reaction rims, (c) qtz microstructures and (d) lack of retrograde reactions involving hydrous phases. Al element distribution patterns in opx (Fig. 4) show a decrease (1) towards the grain boundaries and (2) along straight subgrain boundaries (Fig. 5). Pattern (1) is qualitatively consistent with Al diffusion that is too slow to produce a homogeneous element distribution even at peak metamorphic temperatures. Such slow diffusion is consistent with observed Al diffusion only in the boundary regions of opx porphyroclasts up to 960 °C (Furuhso and Kanagawa, 1999) and implies that the Al element signature we see is indeed a high temperature feature. A more quantitative analysis of element signatures is out of the scope of the present study. The Al element pattern (2) suggests that diffusion rates were higher along subgrain boundaries than in the other parts of opx grains. This is consistent higher Al diffusion rates along dislocation cores than within the lattice (i.e.

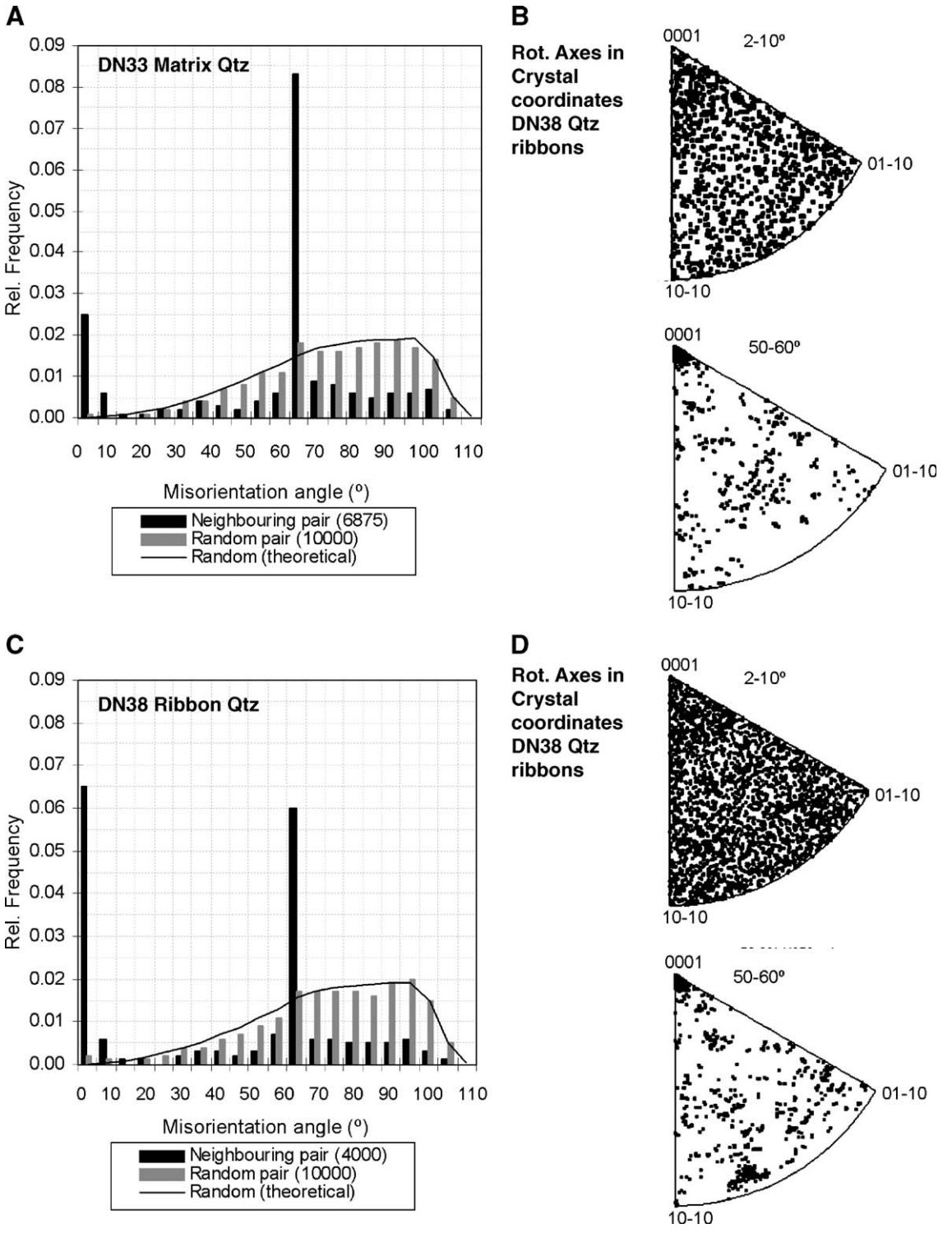

Fig. 10. Misorientation angle distribution and associated rotation axis distribution of matrix qtz grains analysed within sample DN33 (A and B) and grains analysed within qtz ribbons in DN38 (C and D). The theoretical frequency curve is shown as a black line and the two types of misorientation angle distributions are illustrated by block diagrams in dark grey and white, respectively (see text for further explanations). The orientation of the rotation axes are shown in crystal coordinates for misorientation angles less than 10° and the misorientation angle interval between 50° and 70°.

Poirier, 1995). Hence, the deformation that caused the build-up and movement of dislocations to form subgrain boundaries must have been active at near peak metamorphic conditions. As the grt reaction rims in DN38 are undeformed, deformation must have taken place prior to the retrograde reaction that produced these rims, i.e. at high temperatures. Grain boundary geometries of qtz do not show equilibrium microstructures such as 120° triple junctions or any signs of exaggerated grain growth such as a bimodal grain size distribution. The latter feature together with the absence of any retrograde reactions involving hydrous phases, suggest that the dry granulite did not come into contact with external fluids during its exhumation history. Such fluids, though, would be needed in order to increase the grain boundary mobility to a sufficiently high value for any significant microstructural post-deformational and post-peak metamorphic changes i.e. by annealing to take place. This necessity of fluid presence is evidenced by qtz annealing experiments which are always conducted at fluid present conditions (Heilbronner and Tullis, 2002); at completely dry conditions no microstructural changes occur (pers. comm., Tullis, 2001). Therefore, we interpret that the quartz microstructures were not significantly modified during the retrograde exhumation path.

The high abundance of Dauphiné twins is interpreted to indicate crystallographic rearrangement within qtz grains at medium to low temperature. For the formation of Dauphiné twinning two main mechanisms have been suggested: (a) deformation where twins originate mainly in areas of stress concentrations (Lloyd, 1987, 2004) and (b) β to α-qtz phase transition at temperatures around 600–850 °C at P between 1 kbar and 10 kbar (Heaney and Veblen, 1991; Putnis, 1992; Nord, 1994). In our samples observed microstructures do not support a link between stress concentrations e.g. grain asperities and Dauphiné twins, thus we favour the origin of Dauphiné twins due to the phase transition during cooling. Thus, Dauphiné twins are not directly related to the main deformation event. The observed undulose extinction within some qtz grains may partly be due to high temperature deformation and also partly caused by a necessary crystallographic rearrangement when qtz goes through the β to α-qtz phase transition.

In summary, our microstructural observations show that the main features observed can be attributed to a high temperature deformation event above or around 1000 °C, while post-peak metamorphic alterations are limited to localize unhydrous reactions, formation of Dauphiné twins and weak undulose extinction. This interpretation is in agreement with deformation state II (D_2) of Toyoshima et al. (1999) which is, according to the authors, characterized by foliation and strong opx mineral lineation formation. A schematic summary of the suggested PT deformation path for both investigated samples is given in Fig. 11.

5.2. Ultrahigh temperature deformation mechanisms

5.2.1. Orthopyroxene

In both samples opx grains and grain clusters exhibit a shape preferred orientation forming the mineral lineation, distinct grain size independent crystallographic preferred orientations (Figs. 6 and 7) and a high frequency of low angle boundaries (Fig. 8). The latter two characteristics are consistent with deformation by dislocation creep in opx according to the relationship between deformation mechanisms and microstructural characteristics (see e.g. Table 2 in Fliervoet et al., 1999).

Nevertheless, there are distinct differences between the two samples. In DN33 subgrain boundaries are straight and perpendicular to the common grain elongation parallel to [001]. They form traces parallel to (010) and rotation axes of [010] for rotation angles between 3° and 5° (DN33; Fig. 8). In DN38, though, subgrain boundaries are irregular in shape while still

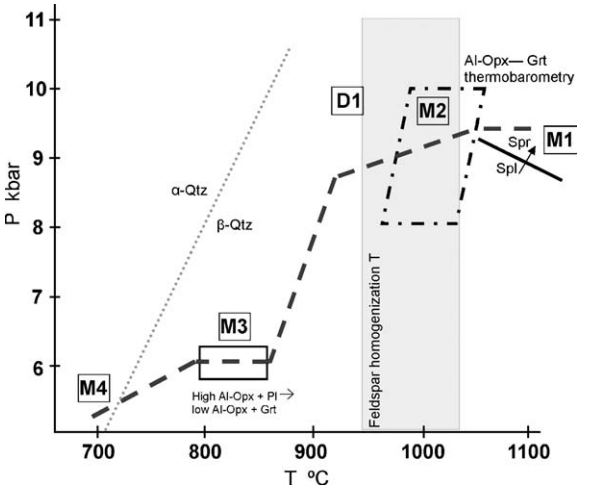

Fig. 11. Schematic PT diagram summarizing thermobarometric estimations (cf. Table 3 and text) according to presented results and former studies. M1: Prograde metamorphic event using spl–spr overgrowth reaction (cf. Eq. (4)). M2: Peak metamorphic conditions estimated by Al–opx–grt thermobarometry (stippled parallelogram) and homogenization temperature of the ternary feldspars (grey field). D1: Deformation event constraint by Al diffusion signatures across subgrains in opx which is interpreted to be closely related to the peak metamorphism (M2), this corresponds to D2 of Toyoshima et al. (1999). M3: Retrogression constrained by grt reaction rims forming around high Al–opx. M4: Substantial evidences of Dauphiné twinning and undulose extinction formation in qtz grains indicate re-structuring at lower temperatures due to the α- to β-qtz transition.

showing a preferred rotation axis of [010]. In addition, between samples different opx preferred crystallographic signatures are documented. In DN33 [010] tilt walls forming straight subgrain boundaries and the character of crystallographic preferred orientation (Fig. 6) agree with dislocation creep dominated by (100)[001] slip. This is the most commonly reported slip system in orthopyroxenes (i.e. Nazé et al., 1987; Ross and Wilks, 1996; Egydio-Silva et al., 2002). This is in contrast with the crystallographic preferred orientation in sample DN38 (Fig. 7) which may be related to an additional active slip system of (010)[001]; this was also reported by Kanagawa et al. (2003) for opx porphyroclasts deformation at temperatures of 650 °C. Nazé et al. (1987), Egydio-Silva et al. (2002) and Ross and Wilks (1996) demonstrated that this slip system exists, though it is more difficult to activate than the more common slip system of (100)[001]. Note that the observed CPO and shape preferred orientation in DN38 could not have been formed by rigid body rotation alone as (a) the grain boundary angle distribution analyses does not show a random angle distribution, (b) there is indeed a preferred rotation axis of [010] and (c) not only individual grain but also grain clusters show the reported results (see above).

Let us consider the possible reasons for the difference in active slip systems in the two samples. Several characteristics of the opx grains are similar in both samples and cannot therefore account for the difference in active slip systems. These similarities are: (a) grain size, (b) grain shape, (c) overall volume proportion and (d) metamorphic conditions of deformation. The main possible differences are (1) Al content of opx and (2) opx–qtz spatial distribution. The Tschermak's substitutions of Al into opx structure introduce systematic changes in the crystal lattice constraining the tetrahedral coordinated Al in one of the tetrahedral chains of the structure and the octahedral coordinated Al in the larger of the octahedral coordination polyhedra, M1, (Molin, 1989; Lund, 2004). Accordingly, coupled substitution of Al equally affects the crystal bonds within and across (010) and no easy translation planes are apparently developed in high Al opx. Hence, Al content cannot directly be related to the observed difference in active slip systems.

In DN33 opx is found in monomineralic bands of large opx grain clusters separated by a quartzo–feldspathic matrix (Fig. 2A) while, in contrast, in DN38 individual and weakly clustered opx grains are situated within a quartzo–feldspathic matrix (Fig. 3). We suggest that individual and loosely clustered opx grains that are "floating" in a qtz–fsp matrix are subject to higher differential stresses at their boundaries than those within monomineralic opx bands. In monomineralic bands, high stresses only occur at the borders of the band boundary while within the band differential stresses are much lower. Therefore, only a small percentage of the grain area is subject to high differential stress. These higher differential stresses that occurred in DN38 may have activated the additional slip system (010)[001].

5.2.2. Quartz

Two types of qtz grains are observed: (a) lobate, elongate matrix grains present in both samples and (b) qtz grains within ribbons exhibiting cuspate boundaries present in DN38. The observed lobate shape of qtz grains, the high frequency of interphase boundaries, the lack of systematic subgrain boundaries and any crystallographic preferred orientation are consistent with diffusion creep as the main deformation mechanism. The presence of a weak to random CPO and misorientation distribution has, for example, also been interpreted as a result of diffusion creep by Fliervoet et al. (1999). A high frequency of interphase boundaries is advantageous for diffusion creep as along such boundaries diffusion is faster than between like–like i.e. qtz–qtz boundaries (Renard et al. (2001). Furthermore, data and interpretations of Martelat et al. (1999) and Gower and Simpson (1992) who argued that cuspate boundary microstructures between elongate qtz grains and feldspars are indicators of high grade diffusion creep. Note that we attribute some of the observed undulose extinction in some qtz grains to retrogression and not to high temperature deformation (see Section 5.1).

Our interpretation of high temperature diffusion creep in qtz is consistent with the experimental results of Brodie and Rutter (2000) who showed that diffusion creep is possible at 1000 °C, strain rates of 3×10^{-14} s^{-1}, low differential stresses (<1 MPa) and grain sizes of ~100 μm. In the present samples the grain size of the analysed matrix quartz grains ranges from 50 μm to 200 μm. Even qtz grains and subgrains in ribbons, which are partly larger than the matrix grains, show a random CPO (Fig. 9) which suggesting significant influence from diffusion creep. Thus, at ultrahigh temperatures flow behaviour of qtz is Newtonian and only low differential stresses can be supported (Paterson and Luan, 1990; Brodie and Rutter, 2000). However, the high frequency of subgrain boundaries within ribbons is indicative of simultaneous dislocation creep. The latter maybe a direct effect of larger grain sizes found in the quartz ribbons.

Substantial evidences of dauphine twinning and undoluse extinction or subgrains in qtz grains indicate restructuring at lower temperatures and in the T range of the α to β-qtz transition.

5.3. Implications on the rheology of felsic rocks at lower crustal conditions

Our detailed microstructural observations of ultrahigh temperature and medium to high pressure granulites and their interpretation in terms of active deformation mechanisms give some insight into the type of rheology can be expected at lower crustal conditions. If quartz is the mineral phase governing the rock rheology, Newtonian flow behaviour is expected and only low differential stress can be supported. However, if the stress supporting mineral phase is orthopyroxene, the flow law resulting from dislocation creep will govern the rheology of the rock unit; hence, an exponential relationship between stress and strain rate at medium to high stress is to be expected. At present, it is not possible to predict the rheology of a "common" felsic lower crustal rock. For that, the mineral phase distribution needs to be considered. As suggested by the activation of slip systems in opx, the spatial distribution of mineral phases influences the type and character of activated deformation mechanisms. In addition, the amount and arrangement of different mineral phases governs which of the phases is stress supporting. Already some studies have tried to tackle this problem (e.g. Handy, 1990, 1994), but in order to resolve the effect of the spatial distribution of minerals that deform due to different deformation mechanisms on the bulk rheology of the rock additional approaches are necessary. For example, numerical simulations such as using the numerical system Elle (Jessell et al., 2001) coupled both with additional detailed analysis of outcrops and microstructures of a variety of rocks and with studies of other mineral phases such as feldspar that have deformed at the same PT fluid conditions but with different spatial distributions will be needed.

6. Summary and conclusions

In this study, we present detailed microstructural evidence for deformation of qtz and opx at ultrahigh temperatures (~1000 °C at 8–10 kbar). Results show the formation of crystallographic preferred orientation and subgrain boundaries in opx, which is consistent with deformation of opx by dislocation creep. Furthermore, two different slip systems are activated in the two samples in response to different differential stresses imposed. This difference originates from the variation in spatial distribution of opx grains and matrix qtz and fsp. In monomineralic opx bands, the active slip system is dominated by (100)[001] and subgrains form straight [010] tilt walls. In contrast, in opx grains that are situated within a quartzo–feldspathic matrix the additional slip system (010)[001] which requires higher differential stresses, is activated. Quartz microstructures, such as the absence of both crystallographic preferred orientation and any systematic subgrain boundaries, point to deformation dominated by diffusion creep even at grain sizes as large as 200 μm. Larger qtz grains within ribbons show a grain size dependent increase in the frequency of subgrain boundaries indicating an increased influence of deformation by dislocation creep besides the dominant diffusion creep. According to our results we interpret that higher differential stresses can only be supported by a rock in which opx is stress supporting and this results an exponential stress strain rate relationship at medium to high stresses, while in quartz dominated rocks only low stresses are supported and the flow is Newtonian. The activation of different slip systems and the dominance of different deformation mechanisms are influenced by heterogeneous phase (and hence stress and strain) distribution and as such this has a significantly influence on the rock rheology. The exact correlation of these parameters on the rheology of the rock units concerned needs to be addressed in future studies.

Acknowledgements

ML acknowledges the financial help of "Kontorchef Waldemar Paulsen og Hustru Edel Paulsens mindefond" for the financial support and Aalborg University, Denmark, for making the facilities available for use during the writing process of this study. We are grateful to Prof. Harley for the provision of the two samples and to Prof. Prior for welcoming the authors in his laboratory. We thank P. Trimby for the helpful comments on earlier versions of this manuscript. Critical comments and notes from Prof. Kanagawa and an anonymous reviewer greatly improved the manuscript. SP acknowledges financial support by the Marie Curie Fellowship HPMF-CT-2001-01457. The CamScan X500 was funded by HEFCE through the grant JR98LIPR. SLH acknowledges Dr Daniel Dunkley for the collection and provision of samples DN33 and DN38, and JARE (Japanese Antarctic Research Expedition) for field and logistic support with JARE 40 in Enderby Land 1998–1999.

References

Aranovich, L. Ya., Berman, R.G., 1997. A new garnet–orthopyroxene barometer based on reserved Al_2O_3 solubility in FeO-Al_2O_3-SiO_2. American Mineralogist 82, 345–353.

Bhattacharya, A., Krishnakumar, K.R., Raith, M., Sen, S.K., 1991. An improved set of a-X parameters for Fe-Mg-Ca garnets and

refinements of the orthopyroxene–garnet thermometer and the orthopyroxene–garnet–plangioclase quartz barometer. Journal of Petrology 32, 629–656.

Brodie, K.H., Rutter, E.H., 2000. Deformation mechanisms and rheology: why marble is weaker than quartzite. Journal of the Geological Society 157, 1093–1096.

Carswell, D.A., Harley, S.L., 1989. Mineral barometry and thermometry. In: Carswell, D.A. (Ed.), Eclogites and Related Rocks. Blackie, Glasgow, pp. 83–110.

Carter, N.L., Tsenn, M., 1987. Flow properties of the contiential lithosphere. Tectonophysics 136, 27–63.

Egydio-Silva, M., Vauchez, A., Bascou, J., Hippertt, J., 2002. High-temperature deformation in the Neoproterozoic transpressional Ribbeira belt, southeast Brazil. Tectonophysics 352, 203–224.

Ellis, D.J., 1980. Osumilite–sapphirine–quartz granulites from Enderby Land, Antarctica: *P–T* conditions of metamorphism, implications for garnet–cordieriete equilibria and the evolution of the deep crust. Contributions to Mineralogy and Petrology 74, 201–210.

Ellis, D.J., 1987. Origin and evolution of granulites in normal and thickened crusts. Geology 15, 167–170.

Fliervoet, T.F, Drury, M.R., Chopra, P.N., 1999. Crystallographic preferred orientations and misorientation in some olivine rocks deformed by diffusion or dislocation creep. Tectonophysics 303, 1–28.

Frost, H.J., Ashby, M., 1983. Deformation-Mechanism Maps: the Plasticity and Creep of Metals and Ceramics. Pergamon Press, Oxford.

Fuhrmann, M.L., Lindsley, D.H., 1988. Ternary-feldspar modelling and thermobarometry. American Mineralogist 73, 201–215.

Furuhso, M., Kanagawa, K., 1999. Transformation-induced strain localization in a lherzolite mylonite from the Hikada metamorphic belt of central Hokkaido, Japan. Tectonophysics 313, 411–432.

Ganguly, J., Cheng, W., Tirone, M., 1996. Thermodynamics of aluminosilicate garnet solid solution: new experimental data, an optimized model, and thermometric applications. Contributions to Mineralogy and Petrology 126, 131–151.

Gower, R.J.W., Simpson, C., 1992. Phase boundary mobility in naturally deformed, high-grade quartzo–feldspathic rocks: evidence for diffusional creep. Journal of Structural Geology 14, 301–313.

Handy, M.R., 1990. The solid-state flow of polymineralic rocks. Journal of Geophysical Research 95, 88647–88661.

Handy, M.R., 1994. Flow laws for rocks containing two non-linear viscous phases: a phenomenological approach. Journal of Structural Geology 16, 287–301.

Harley, S.L., 1984. An experimental study of the partitioning of Fe and Mg between garnet and orthopyroxene. Contributions to Mineralogy and Petrology 86, 359–373.

Harley, S.L., 1985. Garnet–orthopyroxene bearing granulites from Enderby Land, Antarctica: metamorphic pressure–temperature–time evolution of the Archean Napier Complex. Journal of Petrology 26, 819–856.

Harley, S.L., 1987. A pyroxene-bearing meta-ironstone and other pyroxene–granulites from Tonagh Island, Enderby Land, Antarctica: further evidence for very high temperature (>980 °C) Archean regional metamorphism in the Napier Complex. Journal of Metamorphic Geology 5, 341–356.

Harley, S.L., 1989. The origin of granulites: a metamorphic perspective. Geological Magazine 126, 215–247.

Harley, S.L., 1998. Ultrahigh temperature granulite metamorphism (1050 °C, 12 kbar) and decompression in garnet (Mg70)-orthopyroxene–sillimanite gneisses from Rauer Group, East Antarctica. Journal of Metamorphic Geology 16, 541–562.

Harley, S.L., Green, D.H., 1982. Garnet–orthopyroxene barometry for granulites and peridotites. Nature 300, 697–701.

Harley, S.L., Hensen, B.J., 1990. Archean and Proterozoic high-grade terrains of East Antarctica (40–80° E): a case study of diversity in granulite facies metamorphism. In: Asworth, J.R., Brown, M. (Eds.), High temperature Metamorphism and Crustal Anatexis. Unwin Hymman, London, pp. 320–370.

Harley, S.L., Motoyoshi, Y., 2000. Al zoning in orthopyroxene in a sapphirine quartzite: evidence for >1120 °C UHT metamorphism in the Napier Complex, Antarctica, and implications for the entropy of sapphirine. Contributions to Mineralogy and Petrology 138, 293–307.

Heaney, P.J., Veblen, D.R., 1991. Observations of the α–β phase transition in quartz: a review of imaging and diffraction studies and some new results. American Mineralogist 76, 1018–1032.

Heilbronner, R., Tullis, J., 2002. The effect of static annealing on microstructures and crystallographic preferred orientations of quartzites experimentally deformed in axial compression and shear. Geological Society of London, Special Publication 200, 191–218.

Hokada, T., 2001. Feldspar thermometry in ultrahigh-temperature metamorphic rocks: evidence of crustal metamorphism attaining ~1100 °C in the Archean Napier Complex, East Antarctica. American Mineralogist 86, 932–938.

Jessell, M., Bons, P., Evans, L., Barr, T., Stüwe, K., 2001. Elle: the numerical simulation of metamorphic and deformation microstructures. Computers and Geosciences 27, 17–30.

Kanagawa, K., Shimano, H., Tanaka, Y., Development of gabbro mylonite in the lower crust: an example of the Pankenushi gabbro mylonite in central Hokkaido, Japan. Poster publication, DRT 2003, St. Malo.

Kretz, R., 1983. Symbols of rock-forming minerals. American Mineralogist 68, 277–279.

Lloyd, G.E., 1987. Atomic number and crystallographic contrast images with the SEM: a review of backscatter techniques. Mineralogical Magazine 51, 3–19.

Lloyd, G.E., 2004. Microstructural evolution in a mylonititic quartz simple shear zone: the significant roles of Dauphiné twinning and misorientation. Geological Society of London, Special Publication 224, 39–61.

Lund, M., 2004. Microfabric and Deformation Mechanisms in deformed high grade granulites: A combined study using X-ray diffraction, microprobe and electron backscatter diffraction analyses. Master Thesis, University of Copenhagen.

Martelat, J.E., Schulmann, K., Lardeaux, J.M., Nicollet, C., Cardon, H., 1999. Granulite microfabrics and deformation mechanisms in southern Madagascar. Journal of Structural Geology 21, 671–687.

Molin, G.M., 1989. Crystal-chemical study of cation disordering in Al-rich and Al-poor orthopyroxenes from spinel lherzolite xenoliths. American Mineralogist 74, 593–598.

Nazé, L., Doukhan, N., Doukhan, J.-C., Latrous, K., 1987. A TEM study of lattice defects in naturally and experimentally deformed orthopyroxenes. Bulletin of Mineralogy 110, 497–512.

Nord, G.L., 1994. Transformation-induced twin boundaries in minerals. Phase Transitions 48, 107–134.

Osanai, Y., Toyoshima, T., Owada, M., Tsunogae, T., Hokada, T., Crowe, W., 1999. Geology of ultrahigh-temperature metamorphic rocks from Tonagh Island in the Napier Complex, East Antarctica. Polar Geoscience 12, 1–28.

Paterson, M.S., Luan, F.C., 1990. Quartzite rheology under geological conditions. Geological Society of London, Special Publication 54, 299–307.

Poirier, J.P., 1995. Plastic rheology of crystals. Mineral Physics and Crystallography. A Handbook of Physical Constants; AGU Reference Shelf, vol. 2, pp. 237–247.

Putnis, A., 1992. Introduction of Mineral Sciences. Cambridge University Press, Cambridge, p. 457.

Renard, F., Dysthe, D., Feder, J., Bjørlykke, K., Jamtveit, B., 2001. Enhanced pressure solution creep rates induced by clay particles: experimental evidence in salt aggregates. Geophysical Research Letters 28, 1295–1298.

Ross, J.V., Wilks, K.R., 1996. Microstructure development in an experimentally sheared orthopyroxene granulite. Tectonophysics 256, 83–100.

Sheraton, J.W., Offe, L.A., Tingey, R.J., Ellis, D.J., 1980. Enderby Land, Antarctica — an unusual Precambrian high-grade metamorphic terrain. Journal of the Geological Society of Australia 27, 1–18.

Sheraton, J.W., Tingey, R.J., Black, L.P., Offe, L.A., Ellis, D.J., 1987. Geology of Enderby Land and Kemp Land Antarctica. BMR Bulletin 223, 1–51.

Toyoshima, T., Osanai, Y., Owada, M., Tsunogae, T., Hokada, T., Crowe, W., 1999. Deformation of ultrahigh-temperature metamorphic rocks from Tonagh Island in the Napier Complex, East Antarctica. Polar Geoscience 12, 29–48.

Wen, S., Nekvasil, H., 1994. SOLVCALC: an interactive graphics program package for calculating the ternary feldspar solvus and for two-feldspar geothermometry. Computers and Geosciences 20, 1025–1040.

Wheeler, J., Prior, D.J., Jiang, Z., Spiess, R., Trimby, P.W., 2001. The petrological significance of misorientations between grains. Contributions to Mineralogy and Petrology 141, 109–124.

Wood, B.J., 1974. The solubility of alumina in orthopyroxene coexisting with garnet. Contributions to Mineralogy and Petrology 46, 1–15.